

What can we learn from nonequilibrium response of a strange metal?

B.A. Polyak,¹ V.S. Khrapai,^{1,2} and E.S. Tikhonov^{1,3,*}

¹*Osipyan Institute of Solid State Physics RAS, 142432 Chernogolovka, Russian Federation*

²*National Research University Higher School of Economics,
20 Myasnitskaya Street, Moscow 101000, Russian Federation*

³*Laboratory for Condensed Matter Physics, HSE University, Moscow, 101000 Russia*

We critically address the recent experiment [1] on nonequilibrium transport and noise in a strange metal YbRh_2Si_2 patterned into the nanowire shape. In the long device, resistivity, differential resistance and current noise data seem to be consistent allowing us to extract electron-phonon coupling and the temperature dependence of electron-phonon scattering length. The obtained values can be reconciled with the experimental data for the short device only assuming the significant contact resistance. We discuss its possible origin as due to the current redistribution between YbRh_2Si_2 and its gold covering, and reveal that this redistribution contact resistance should be proportional to the YbRh_2Si_2 resistivity. We also discuss some subtleties of the noise measurements. Overall, neglecting electron-phonon energy relaxation even in the shortest devices is arguable so that the observed shot noise suppression can hardly be attributed to the failure of quasiparticle concept.

The origin of strange metal behavior which is manifested in the linear temperature (T) dependence of resistivity down to lowest T in some materials [2–6], remains without generally accepted theoretical explanation [7–13]. On the experimental side, beyond common resistivity measurements novel approaches [1, 14, 15] are required. In particular, the recent paper by Liyang Chen et al. [1] reports on the measurements of shot noise in the heavy fermion strange metal YbRh_2Si_2 patterned into the nanowire shape. The authors claim that the observed shot noise suppression can not be attributed to the electron-phonon energy relaxation in a standard Fermi liquid model but rather indicates the failure of quasiparticle concept. This interpretation has been criticized [16, 17] which motivated us to discuss in the present manuscript the peculiarities of the nonequilibrium transport approach to the study of strange metals.

Fig. 1(a) demonstrates the sketch of studied devices. Patterned from a $t = 60$ nm thick YbRh_2Si_2 film (gray) with resistivity ρ , grown on germanium substrate, they are represented by nanowire-shaped constrictions of length L and width w , connected to source and drain pads. As shown by yellow shading, these two pads are additionally covered with 200 nm of gold. We note that at low bath temperature (T_0) the gold conductivity is approximately 10 times higher than that of YbRh_2Si_2 (at 3 K). Bottom part of Fig. 1(a) shows schematically the current density vector both in YbRh_2Si_2 and in gold covering in the region where current redistributes between the two layers. This region extends for the so-called current transfer length λ depending on the quality of the $\text{YbRh}_2\text{Si}_2/\text{Au}$ interface which we quantify with the interface conductance per unit area, σ_{int} . Overall, the authors provide data for three devices with short constrictions, $L \lesssim 1 \mu\text{m}$, further referred to as short devices, and for one device with long

constriction, $L = 28 \mu\text{m}$, further referred to as long device. The widths of all nanowires range from 140 nm to 300 nm. We estimate geometric dimensions of all constrictions from the available scanning electron micrograph images. As we argue in this manuscript, geometry of the devices may require taking into account the contribution to the measured resistance and noise not only from the nanowires themselves but also from the significant part of the pads.

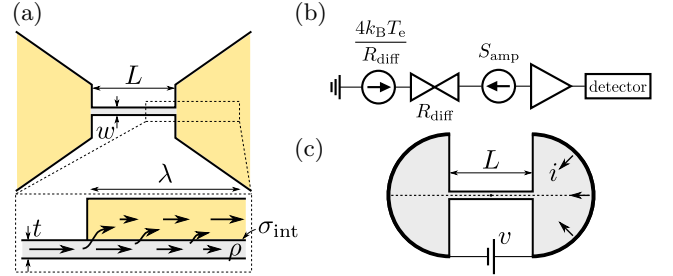


FIG. 1. Device geometry and measurement setup. (a) Schematic representation of a device. YbRh_2Si_2 film $t = 60$ nm thick (gray) is patterned into a constriction connecting two pads. These pads are additionally covered with 200 nm of gold (yellow). The length and the width of the constriction are L and w , respectively. Interface between YbRh_2Si_2 and gold is characterized by conductivity σ_{int} , current transfer length is λ . (b) Geometry used in numerical modelling. We calculate the total current through the constriction, i , in response to the applied bias voltage, v . (c) Equivalent circuit of noise measurement setup.

We start our discussion with the analysis of experimental data for the long device. Here, the central constriction is approximately 30 times longer than that for three short devices so that the possible effect of the interface may be most likely neglected. Below we show that electron-phonon scattering length in YbRh_2Si_2 is $l_{\text{e-ph}}(3\text{K}) \approx 1 \mu\text{m}$ and decreases with increasing temperature. This ensures that besides short regions near the pads, in the

* e-mail:tikhonov@issp.ac.ru

presence of bias current I electron system in the long constriction is described by position-independent electronic temperature $T_e(I)$. At all T_0 this dependence can be obtained using a standard procedure. From the differential resistance data provided in Supplementary Materials (SM) Fig.S3B [1], we extract $R = V/I$ at $T_0 = 3\text{K}$, 5K and 7K . Further, attributing the growth of $R(I)$ with increasing current to the increase of T_e , we extract $T_e(I)$. Here, we use the fact that the T -dependence of the normalized resistance of the devices is demonstrated to be the same as that for the unpatterned film, see Fig.1C [1]. The obtained curves $T_e(I)$ are shown in Fig. 2(a). Without noise measurements, these data already allow one to estimate electron-phonon coupling which describes the power flow from electron to phonon subsystem via

$$P_{e\text{-ph}} = V\Sigma_{e\text{-ph}}(T_e^n - T_{\text{ph}}^n),$$

where V is the system volume and the exponent n typically varies in the range $n \approx 3 - 5$ [18]. The devices are patterned on crystalline germanium substrates ensuring $T_{\text{ph}} = T_0$. In a steady state $P_{e\text{-ph}} = P_J$, where P_J is the released Joule heat power so that

$$P_J = V\Sigma_{e\text{-ph}}(T_e^n - T_0^n). \quad (1)$$

In Fig. 2(b) we show that $n = 4.7$ fits the data perfectly with $\Sigma_{e\text{-ph}} = 9.6 \cdot 10^8 \text{ W/K}^{4.7} \text{ m}^3$ (we take $w = 300 \text{ nm}$). From here, we extract the T -dependence of the electron-phonon scattering length using [19]

$$l_{e\text{-ph}} = L [\mathcal{L}/nT^{n-2}\Sigma_{e\text{-ph}}R(T)]^{1/2},$$

where $\mathcal{L} = 2.44 \cdot 10^{-8} \text{ W}\Omega\text{K}^{-2}$ is the Lorenz number. The result is shown in Fig. 2(c) and in the given temperature range can be reasonably approximated as $l_{e\text{-ph}} \propto T^{-1.7}$, see the dashed line. Importantly, $l_{e\text{-ph}}(3\text{K}) \approx 1.4 \mu\text{m}$ ensuring the possibility to introduce position-independent electronic temperature $T_e(I)$ which will be further used in noise treatment.

Before discussing nonequilibrium noise of the long device, we note some general details of the noise measurements. In the setup used in [1], see Fig. 1(b) for the schematic circuit, the voltage noise before amplification is determined by two contributions,

$$S_V(I) = \left[\frac{4k_B T_e(I)}{R_{\text{diff}}(I)} + S_{\text{amp}} \right] R_{\text{diff}}^2(I), \quad (2)$$

where the first term comes from the current noise of the device itself, the second term is defined by the parasitic input current noise of the amplifiers and $S_V(0)$ is the voltage noise in equilibrium. Note that in the nonlinear regime R_{diff} depends on I so that S_{amp} contributes to the measured excess voltage noise. Whether one can neglect S_{amp} or not, depends on the interplay between the two terms in (2). Therefore, along with determining the gain it is also the goal of calibration to get the magnitude of amplifier noise. Typically, when one uses homemade

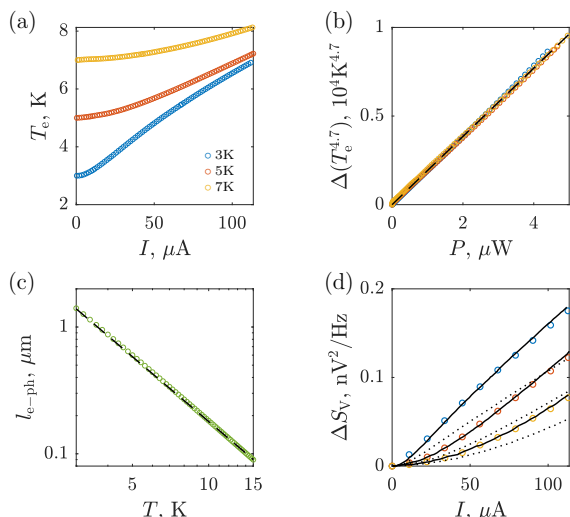


FIG. 2. Nonequilibrium response of the long nanowire. (a) Electronic temperature of the nanowire as a function of bias current. (b) Electron-phonon power flow obeys $P = \Sigma_{e\text{-ph}}(T_e^{4.7} - T_{\text{ph}}^{4.7})$ with $\Sigma_{e\text{-ph}} = 9.6 \cdot 10^8 \text{ W/K}^{4.7} \text{ m}^3$. (c) Electron-phonon scattering length as a function of temperature. Dashed line is $l_{e\text{-ph}} \propto T^{-1.7}$. (d) Voltage noise spectral density of the device. Symbols represent the data from the experiment [1]. Both dotted and dashed lines correspond to $\Sigma_{e\text{-ph}} = 9.6 \cdot 10^8 \text{ W/K}^{4.7} \text{ m}^3$ but with $S_{\text{amp}} = 0$ and $S_{\text{amp}} = 5 \cdot 10^{-25} \text{ A}^2/\text{Hz}$, respectively.

voltage amplifier at liquid helium temperature, its input current noise is on the order of $10^{-27} \text{ A}^2/\text{Hz}$ [20–22] where the precise value depends on the used transistor, operating frequency and device resistance [23]. The authors of [1] use room-temperature commercial preamplifiers, low-noise LI-75, and SR-560 which is usually not used in noise measurements. One can therefore expect $S_{\text{amp}} \gtrsim 10^{-25} \text{ A}^2/\text{Hz}$. We note that unless few orders of magnitude larger, this current noise can not be extracted from the setup calibration discussed in SM section 2 [1]. Namely, the calibration was performed by detecting the room temperature thermal noise of a variety of resistors, see SM Fig.S1. At room temperature, the current noise of a typical used 100Ω resistor is $1.6 \cdot 10^{-22} \text{ A}^2/\text{Hz}$ and by far exceeds the expected value of S_{amp} so that the presented calibration procedure is absolutely helpless in its determination. At the same time, the current noise of a strange metal long device cooled down to 5K and with a resistance of approximately 300Ω is $9 \cdot 10^{-25} \text{ A}^2/\text{Hz}$ which may easily be comparable to the expected value of S_{amp} . In other words, the setup calibration is performed for the values of current noise which are two orders of magnitude greater than those utilized in the experiment.

The value of S_{amp} in the experiment can be estimated by comparison of experimental results for the voltage fluctuations of the long device, see SM Fig.S3A of [1], to what one can expect based on the obtained curves $T_e(I)$ presented in Fig. 2(a). By solid lines in Fig. 2(d) we

show the best fits to the experimental data (symbols) of [1]. These fits are obtained using (2) with $S_{\text{amp}} = 5 \cdot 10^{-25} \text{ A}^2/\text{Hz}$ which perfectly falls in the above order of magnitude expectation. We emphasize that considering current noise of the device in the form of thermal noise with electronic temperature elevated above bath temperature in (2) is valid in the presence of strong electron-phonon scattering. Dotted lines additionally illustrate the fits obtained with zero preamplifier noise. Note these fits go below the experimental data indicating contribution of the parasitic noise.

As a final remark, we note that the obtained above T -independent value of $\Sigma_{\text{e-ph}}$ implies the temperature dependence of $\Gamma = (e/k_{\text{B}})^2 \Sigma_{\text{e-ph}}/\sigma$ since conductivity changes by approximately 40% in the temperature range from 3 K to 7 K. At the same time, the authors of [1] used in their fits T -independent $\Gamma \approx 9 \cdot 10^9 \text{ K}^{-3} \text{ m}^{-2}$, see section 5 in SM. This difference may explain the better quality of our fits for the differential resistance.

We now discuss the short device ($L = 660 \text{ nm}$) presented in the main text, see Fig.2A [1]. Given the width of the constriction is close to that of the long nanowire, one might have expected its linear response resistance at 3 K to be around 6Ω . The actual value is 36Ω demonstrating there is significant inconsistency between formally extracted resistivities of the two devices. Note that additional data on two more short devices presented in SM Fig.S5 reveal the similar discrepancy. In principle, this inconsistency can partly be attributed to the nanoscale patterning of the devices using reactive ion etching which inevitably damages the edges of the constrictions [24]. Fig.1(C,D) of [1] compares temperature and magnetic field (B) behavior of the unpatterned film with that of the nanowire-patterned device and demonstrates similar results in terms of normalized resistances. Therefore, while there is approximately 6-fold difference in the resistivities we believe that the underlying physics is still there so that damaged edges are hardly responsible for the discussed inconsistency. The authors of [1] use Fig.1(C,D) to claim that the total resistance of the device is dominated by the constrictions and the pads contribution is negligible. Below we explain that this argument is in fact incorrect and the pads contribution, which we further refer to as contact resistance, can not be excluded based on the observation of similar for the film and for the patterned devices $R(T)$ and $R(B)$ dependences.

To illustrate the idea, we consider the geometry depicted in the bottom part of Fig. 1(a). Further, we take gold conductivity to be infinitely large. Upon leaving the constriction, current starts to redistribute between the YbRh_2Si_2 film and the gold cover. This redistribution stops after going distance λ deep inside the pad along the interface. This distance is called the current transfer length and depends on the film resistivity and on the interface conductivity, σ_{int} . For $\sigma_{\text{int}} = 0$ current doesn't flow over the interface and remains completely in the YbRh_2Si_2 film. In this case, the contact resistance is log-divergent with the contact size a

as $R_1(a) = \rho \ln(2a/w)/(\pi t)$. On the other hand, if all voltage drop occurs across the interface between the two layers, which happens for $\rho = 0$, the contact resistance is $R_2(a) = 2/(\pi a^2 \sigma_{\text{int}})$. In an infinite contact with both ρ and σ_{int} finite, the reasonable quantitative estimate for both the current transfer length and the contact resistance is obtained from $R_1(\lambda) = R_2(\lambda) \sim R_{\text{cont}}$, that is

$$\frac{\rho}{\pi t} \ln\left(\frac{2\lambda}{w}\right) = \frac{2}{\pi \lambda^2 \sigma_{\text{int}}} \sim R_{\text{cont}}.$$

In Supplemental Material we provide the analytical solution and demonstrate that in the limit of large enough $\lambda \gg w$ the above estimate reproduces the exact result up to only a 10% correction for the logarithm argument. Importantly, the T -dependence of λ is weak and closely follows $\lambda \propto \rho^{-1/2}$. Therefore, up to an unimportant log-factor the contact resistance is proportional to the YbRh_2Si_2 resistivity,

$$R_{\text{cont}} \propto \rho. \quad (3)$$

As a result, observation of the identical T and B response for the parent film and for the patterned device doesn't ensure negligible contact resistance. We also note that for the realistic finite-size devices contact resistance may further be enlarged due to the factors not considered in this idealized picture. In Supplemental Material we show that the T -dependence of linear-response resistance for the short device presented in the main text, see Fig.2A [1], is reasonably approximated using $\lambda(3 \text{ K}) \approx 280 \mu\text{m}$ which is comparable to the pads size and indicates the possible importance of current redistribution effect.

Given the great difference between the expected and the observed resistance of short devices, we argue that the current transfer length may exceed the dimensions of constrictions by orders of magnitude and be comparable to or even exceed the dimensions of devices with pads included. To numerically simulate the differential resistance, we choose the geometry of Fig. 1(c). Here, the radius of pads equals $20 \mu\text{m}$ and the current redistribution on the lateral scale of these pads is neglected. The electrodes are indicated by thick black lines. On the one hand, this geometry is close to the geometry of the patterned film nearby the constriction in real devices. On the other hand, the scale of $20 \mu\text{m}$ is large enough to capture the nonlinearity of differential resistance, since due to $l_{\text{e-ph}} \lesssim 1 \mu\text{m}$ electronic temperature in the presence of current reaches the value of T_0 on the spatial scale of few micrometers beyond the constriction. Additionally, crucial to the numerical calculations for this highly nonuniform geometry, thus chosen size is not too large to require inadequate computing power.

We first implement our numerical approach for the long device. Symbols in the top panel of Fig. 3(a) reproduce the experimental data from the SM Fig.S3B [1]. Solid lines are fits obtained with $\Sigma_{\text{e-ph}} = 6.1 \cdot 10^8 \text{ W/K}^5 \text{ m}^3$ and $n = 5$ in (1) and the T -dependence of YbRh_2Si_2 resistivity $\rho(T) = 10.8 + 1.67 T [\mu\Omega \cdot \text{cm}]$ which captures

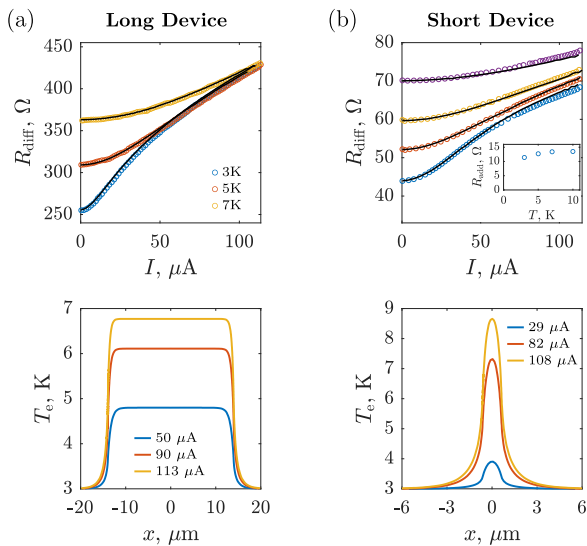


FIG. 3. Numerical simulation of nonequilibrium response for both (a) long and (b) short (device #3) constrictions. Symbols in top panels reproduce the experimental results of [1]. Solid lines are fits obtained with numerical simulation (see text). The inset of top panel in (b) demonstrates the T -dependence of the bias-independent contact resistance. The bottom panels demonstrate the spatial profile of electronic temperature along the dashed line depicted in Fig. 1(c).

the linear-response resistance data and fits the data of Fig.1C [1] with better than 10% accuracy in the temperature range below 10 K. Note that the difference between thus obtained Σ_{e-ph} and the value extracted from Fig. 2(b) is due to the slightly different power-law of electron-phonon cooling rate. The spatial profile of electronic temperature along the dashed line depicted in Fig. 1(c) is demonstrated in the bottom panel of Fig. 3(a) with $x = 0$ corresponding to the center of the constriction.

Having extracted Σ_{e-ph} , we attempt to fit the bias dependence of differential resistance for one of short devices. For this purpose we choose the device #3 from SM Fig.S5E [1]. Among the overall presented three short devices, this is the narrowest one so that we expect the contact resistance to be significant enough but not dominating over the constriction resistance compared with two other short devices. Note also that while the constriction of this device is approximately two times narrower than the constriction of the device #2 from SM Fig.S5(A-C), its resistance is only $\approx 30\%$ greater which again may indicate the significant contact resistance in all short devices. We take the length and the width of the constriction in device #3 to be $l = 1.3 \mu\text{m}$ and $w = 155 \text{ nm}$, respectively; the corresponding resistivity is taken to be the same as for the long device. Symbols in the top panel of Fig. 3(b) reproduce the experimental data from the SM Fig.S5E [1]. Solid lines are

fits obtained with

$$R_{\text{diff}} = \frac{dv}{di} + R_{\text{add}}(T),$$

where v is the voltage applied between two electrodes in Fig. 1(c), i is the calculated current and $R_{\text{add}}(T)$ is chosen as current-independent quantity to fit the linear-response resistance for all four temperatures of interest. R_{add} must include, at least, the contribution to contact resistance due to current redistribution across the imperfect YbRh₂Si₂/gold interface beyond the semicircular pads depicted in Fig. 1(c). Additional contribution to R_{add} may come from finite gold resistivity and possibly present interface defects. Taking into account only current redistribution effect, in accordance with (3) one should expect $R_{\text{add}} \propto \rho$. In the inset we demonstrate the obtained $R_{\text{add}}(T)$ dependence which turns out to be slower than $\rho(T)$ indicating that current redistribution is not the only effect contributing to the contact resistance. Additionally, in the bottom panel of Fig. 3(b) we plot the spatial profile of electronic temperature along the short constriction. Both bottom panels of Fig. 3 verify that electron-phonon scattering is strong enough so that the devices can not be considered as in phase-coherent regime which was recently analyzed theoretically [25].

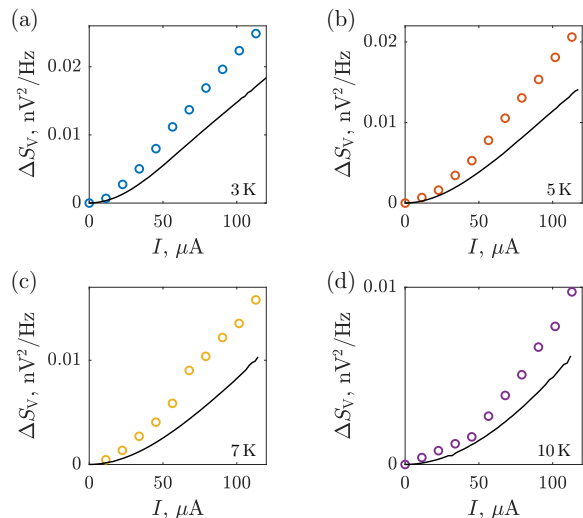


FIG. 4. Numerical simulation of nonequilibrium noise for the device #3. Symbols represent the data from the experiment [1]. Solid lines are fits calculated using the position-dependent electronic temperature from the bottom panel of Fig. 3(b) (see text).

Finally, we compare the experimental results for nonequilibrium noise in the short device with what we expect based on the spatial temperature profile demonstrated in Fig. 3(d). By symbols in Fig. 4 we reproduce the data for the device #3 from SM Fig.S5F [1]. Solid lines are fits calculated using $\Delta S_V = 4k_B T_N (dv/di)$. Here, T_N is the noise temperature of the part of the de-

vice depicted in Fig. 1(c) and calculated using [26]

$$T_N = \frac{\int T(x, y)(\mathbf{j} \cdot \mathbf{E}) dx dy}{\int (\mathbf{j} \cdot \mathbf{E}) dx dy},$$

where \mathbf{j} is the current density and \mathbf{E} is the electric field in the given point of a device. Note that in the above expression for ΔS_V we neglect the nonequilibrium noise of device regions beyond those from Fig. 1(c) as well as the contribution from the amplifier noise due to the device resistance nonlinearity. Importantly, the fits go below the experimental data so that considering the amplifier current noise and the contacts noise may become crucial in interpreting the data.

In conclusion, we discuss the recent strange metal experiment [1] and demonstrate that electron-phonon scattering most likely can not be neglected in the presented short devices which makes the statement on the failure of quasiparticle concept arguable. At the same time, experimental data from the long device contain important information about electron-phonon coupling and the T -dependence of electron-phonon scattering length which is essential for further transport experiments.

We thank Liyang Chen and Douglas Natelson for valuable comments on the device fabrication details. The work is financially supported by RSF Project No. 22-12-00342.

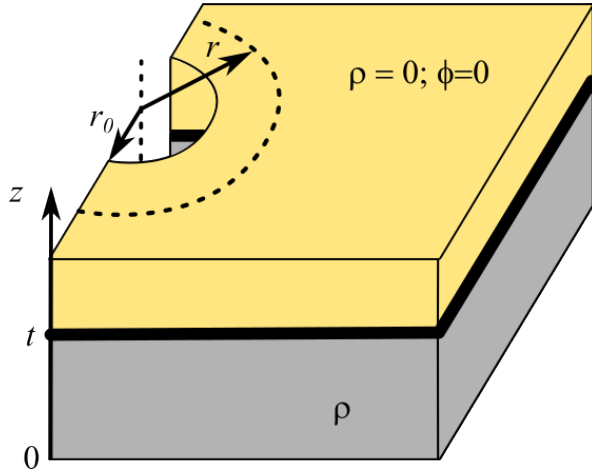
-
- [1] L. Chen, D. T. Lowder, E. Bakali, A. M. Andrews, W. Schrenk, M. Waas, R. Svagera, G. Eguchi, L. Prochaska, Y. Wang, C. Setty, S. Sur, Q. Si, S. Paschen, and D. Natelson, Shot noise in a strange metal, *Science* **382**, 907 (2023).
- [2] H. V. Löhnneysen, T. Pietrus, G. Portisch, H. G. Schlager, A. Schröder, M. Sieck, and T. Trappmann, Non-Fermi-liquid behavior in a heavy-fermion alloy at a magnetic instability, *Physical Review Letters* **72**, 3262 (1994).
- [3] P. Fournier, P. Mohanty, E. Maiser, S. Darzens, T. Venkatesan, C. J. Lobb, G. Czjzek, R. A. Webb, and R. L. Greene, Insulator-Metal Crossover near Optimal Doping in $\text{Pr}_{2-x}\text{Ce}_x\text{CuO}_4$: Anomalous Normal-State Low Temperature Resistivity, *Physical Review Letters* **81**, 4720 (1998).
- [4] A. Legros, S. Benhabib, W. Tabis, F. Laliberté, M. Dion, M. Lizaire, B. Vignolle, D. Vignolles, H. Raffy, Z. Z. Li, P. Auban-Senzier, N. Doiron-Leyraud, P. Fournier, D. Colson, L. Taillefer, and C. Proust, Universal T-linear resistivity and Planckian dissipation in overdoped cuprates, *Nature Physics* **15**, 142 (2019).
- [5] D. H. Nguyen, A. Sidorenko, M. Taupin, G. Knebel, G. Lapertot, E. Schuberth, and S. Paschen, Superconductivity in an extreme strange metal, *Nature Communications* **12**, 4341 (2021).
- [6] A. Jaoui, I. Das, G. Di Battista, J. Díez-Mérida, X. Lu, K. Watanabe, T. Taniguchi, H. Ishizuka, L. Levitov, and D. K. Efetov, Quantum critical behaviour in magic-angle twisted bilayer graphene, *Nature Physics* **18**, 633 (2022).
- [7] V. R. Shaginyan, K. G. Popov, and V. A. Khodel, Quasi-classical physics and T-linear resistivity in both strongly correlated and ordinary metals, *Physical Review B* **88**, 115103 (2013).
- [8] E. H. Hwang and S. Das Sarma, Linear-in- T resistivity in dilute metals: A Fermi liquid perspective, *Physical Review B* **99**, 085105 (2019).
- [9] A. A. Patel and S. Sachdev, Theory of a Planckian Metal, *Physical Review Letters* **123**, 066601 (2019).
- [10] V. R. Shaginyan, M. Ya. Amusia, A. Z. Msezane, V. A. Stephanovich, G. S. Japaridze, and S. A. Artamonov, Fermion Condensation, T-Linear Resistivity, and Planckian Limit, *JETP Letters* **110**, 290 (2019).
- [11] G. E. Volovik, Flat Band and Planckian Metal, *JETP Letters* **110**, 352 (2019).
- [12] M. V. Sadovskii, On the Planckian Limit for Inelastic Relaxation in Metals, *JETP Letters* **111**, 188 (2020).
- [13] M. V. Sadovskii, Planckian relaxation delusion in metals, *Physics-Uspekhi* **64**, 175 (2021).
- [14] Y. Nakajima, T. Metz, C. Eckberg, K. Kirshenbaum, A. Hughes, R. Wang, L. Wang, S. R. Saha, I.-L. Liu, N. P. Butch, D. Campbell, Y. S. Eo, D. Graf, Z. Liu, S. V. Borisenko, P. Y. Zavalij, and J. Paglione, Quantum-critical scale invariance in a transition metal alloy, *Communications Physics* **3**, 181 (2020).
- [15] B. Michon, C. Berthod, C. W. Rischau, A. Ataei, L. Chen, S. Komiya, S. Ono, L. Taillefer, D. Van Der Marel, and A. Georges, Reconciling scaling of the optical conductivity of cuprate superconductors with Planckian resistivity and specific heat, *Nature Communications* **14**, 3033 (2023).
- [16] V. R. Shaginyan, A. Z. Msezane, and G. S. Japaridze, Comment on "Shot noise in a strange metal" (2023), arxiv:2312.16269 [cond-mat].
- [17] B. A. Polyak, E. S. Tikhonov, and V. S. Khrapai, Comment on "Shot noise in a strange metal" (2024), arxiv:2401.08681 [cond-mat].
- [18] F. Giazotto, T. T. Heikkilä, A. Luukanen, A. M. Savin, and J. P. Pekola, Opportunities for mesoscopies in thermometry and refrigeration: Physics and applications, *Reviews of Modern Physics* **78**, 217 (2006).
- [19] A. O. Denisov, E. S. Tikhonov, S. U. Piatrusha, I. N. Khrapach, F. Rossella, M. Rocci, L. Sorba, S. Roddaro, and V. S. Khrapai, Strategy for accurate thermal biasing at the nanoscale, *Nanotechnology* **31**, 324004 (2020).
- [20] M. Reznikov, R. D. Picciotto, T. G. Griffiths, M. Heiblum, and V. Umansky, Observation of quasiparticles with one-fifth of an electron's charge, *Nature* **399**, 238 (1999).
- [21] E. S. Tikhonov, M. Yu. Melnikov, D. V. Shovkun, L. Sorba, G. Biasiol, and V. S. Khrapai, Nonlinear transport and noise thermometry in quasiclassical ballistic point contacts, *Physical Review B* **90**, 161405 (2014).
- [22] T. Muro, Y. Nishihara, S. Norimoto, M. Ferrier, T. Arakawa, K. Kobayashi, T. Ihn, C. Rössler, K. Ensslin, C. Reichl, and W. Wegscheider, Finite shot noise and electron heating at quantized conductance in high-mobility quantum point contacts, *Physical Review B* **93**, 195411 (2016).

- [23] T. Arakawa, Y. Nishihara, M. Maeda, S. Norimoto, and K. Kobayashi, Cryogenic amplifier for shot noise measurement at 20 mK, *Applied Physics Letters* **103**, 172104 (2013).
- [24] L. Chen and D. Natelson, private communication.
- [25] A. Nikolaenko, S. Sachdev, and A. A. Patel, Theory of shot noise in strange metals, *Phys. Rev. Res.* **5**, 043143 (2023).
- [26] S. U. Piatrusha, V. S. Khrapai, Z. D. Kvon, N. N. Mikhailov, S. A. Dvoretzky, and E. S. Tikhonov, Edge states in lateral p - n junctions in inverted-band HgTe quantum wells, *Physical Review B* **96**, 245417 (2017).

Supplemental Material

Below we solve a problem of current spreading in a layered two-dimensional geometry with poor interface. The results evidence that the contact resistance scales similar to the resistivity of the parent film. Numerical simulations are performed to understand possible impact of the interface resistance in Ref. [Liyang Chen et al., Science **382**, 907 (2023)]. The experimental deviations could be explained by such a contact effect.

I. LAYOUT



Supplemental Material Fig. 1. Sketch of a layered contact. Lower grey layer has a finite resistivity (thickness t). Upper yellow layer is an ideal metal, which is grounded. A very thin interface between the two layers is depicted by a black thick line. The interface emulates bad contact and in the presence of current there is a finite voltage drop across the interface.

Fig. 1 represents a model of a layered contact. The upper layer is an ideal metal with infinite conductivity, which is grounded, i.e. its electric potential is $\phi = 0$. The lower layer is a metal with finite conductivity $\sigma = 1/\rho$ and thickness t . The interface between the two metal layers is assumed to have zero thickness and is characterized by a finite conductivity per unit area σ_i . The current inflows the lower layer at the inner radial contact of the radius r_0 . The center of that inner contact is chosen to be the origin of a cylindrical polar coordinate system (r, φ, z) .

II. QUALITATIVE PICTURE

A good estimate of the spreading resistance can be achieved with the following argument. Consider the contact of geometry of Fig. 1 with the inner and outer radii of r_0 and $r_{max} \gg r_0$, respectively. For $\sigma_i = 0$ the current does not flow over the interface and remains in the

lower layer. In this case, the contact resistance has a log-divergence in size: $R_1(r_{max}) = \rho(\pi t)^{-1} \ln(r_{max}/r_0)$. On the other hand, if all the voltage drop occurs across the interface between the two layers, which happens for $\rho = 0$, the contact resistance is $R_2(r_{max}) = 2(\pi r_{max}^2 \sigma_i)^{-1}$. In an infinite contact with both ρ and σ_i non-zero, the current overflows the interface within the region of the radius given by the current transfer length λ . This length can be estimated from $R_1(\lambda) = R_2(\lambda)$. For such λ , the contact resistance can be estimated as:

$$R_c \approx R_1(\lambda) = \frac{\rho}{\pi t} \ln(\lambda/r_0) \quad (S1)$$

III. SOLUTION: HALF-PLANE INFINITE PAD

The spatial distribution of the electric potential is found from a solution of Laplace's equation $\Delta\phi = 0$. Owing to the axial symmetry, the potential is independent of φ and we find the solution of the form $\phi(r, z) = F(r)G(z)$. It then follows from the Laplace's equation:

$$\frac{1}{F} \frac{d^2 F}{dr^2} + \frac{1}{rF} \frac{dF}{dr} = -\frac{1}{G} \frac{d^2 G}{dz^2}, \quad (S2)$$

which implies that the rhs and lhs of this equation equal the same constant, independent of both r and z . This equation is supplemented by the expressions for the current density in the lower metal layer:

$$j_z = -\sigma F(r) \frac{dG}{dz} \quad (S3)$$

$$j_r = -\sigma G(z) \frac{dF}{dr} \quad (S4)$$

The solution for $G(z)$ is straightforward. Assuming $d^2 G/dz^2 = -\gamma^2 G(z)$ and from the boundary condition of $j_z = 0$ at the $z = 0$ plane, we find $G(z) = G_0 \cos(\gamma z)$. The boundary condition at the interface $z = t$ is different. We assume that the interface between the two metals has zero thickness and is characterized by a finite conductivity per unit area σ_i . Hence, the finite voltage drop at the interface is connected to the current density along the z -axis:

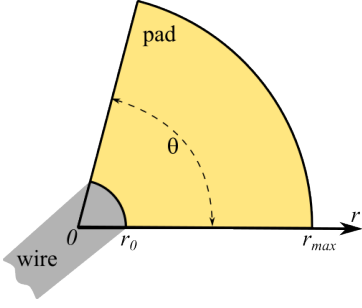
$$\phi(r, z = t - 0) - \phi(r, z = t + 0) = \frac{j_z(r, z = t)}{\sigma_i},$$

where, by assumption, $\phi(r, z = t + 0) = 0$. Together with the solution for $G(z)$ and Eq. (S3) this expression determines γ :

$$\gamma \tan(\gamma t) = \frac{\sigma_i}{\sigma}, \quad (S5)$$

which in the limit of $\gamma t \ll 1$ reduces to $\gamma = \sqrt{\sigma_i/(t\sigma)}$. Note that γ^{-1} has a meaning of current transfer length, i.e. a typical length on which most of the current from the lower layer flows over to the upper layer. Going back to the Eq. (S2), the solution for $F(r)$ is found from:

$$x \frac{d^2 F}{dx^2} + \frac{dF}{dx} - xF = 0, \quad (S6)$$



Supplemental Material Fig. 2. Sketch of a realistic contact pad, shaped as a horn with the inner radius of r_0 and the outer radius of r_{\max} . The color notations are the same as in Fig. 1.

where $x = \gamma r$. The solution of (S6) converging at $x \rightarrow \infty$ is $F(r) = F_0 K_0(\gamma r)$, where K_0 is the Bessel-K function of the zero-th order. From the identity $dK_0(x)/dx = -K_1(x)$, where K_1 is the Bessel-K function of the first order, one finds a solution for the electric potential and radial current density:

$$\phi(r, z) = \phi_0 K_0(\gamma r) \cos(\gamma z) \quad (\text{S7})$$

$$j_r(r, z) = \phi_0 \gamma \sigma K_1(\gamma r) \cos(\gamma z), \quad (\text{S8})$$

where $\phi_0 = F_0 G_0$ is a constant. The resistance R_c of the contact pad depicted in Fig. 1 is calculated easily for $\gamma t \ll 1$. The total current flowing into the contact equals $I = \pi r_0 t \cdot j_r(r = r_0)$, so that:

$$R_c = \frac{1}{\pi \sigma t} \frac{K_0(\gamma r_0)}{\gamma r_0 K_1(\gamma r_0)}, \quad (\text{S9})$$

with $r_0 = w/2$, where w is the width of a wire to which the contact pad is attached. Using that $K_0(x)/x K_1(x) \approx \ln(1.12/x)$ in the limit of $x \rightarrow 0$, one can simplify the Eq. (S9) for $\gamma w \ll 1$:

$$R_c \approx \frac{\rho}{\pi t} \ln\left(\frac{2.24}{\gamma w}\right) \quad (\text{S10})$$

The Eq. (S10) shows that in the case of poor interface ($\gamma w \ll 1$) the contact resistance scales proportional to the material's resistivity ρ . The dependence of γ on σ , see Eq. (S5), is has a minor effect and enters via the log-term. Note that (S10) is very close to the qualitative estimate of (S1) with $\lambda \approx \gamma^{-1}$.

IV. SOLUTION: FINITE HORN-SHAPED PAD

Consider a more realistic geometry of the finite size contact pad that has a shape of a horn. The angular width of the horn is θ and the inner and outer radii are, respectively, r_0 and r_{\max} , see the Fig. 2. In this case the solution of the Eq. (S6) is found from a different boundary condition, namely from $j_r(r = r_{\max}) = 0$, i.e. zero

in-plane current at the outer boundary of the lower layer. In this case $G(z)$ is the same and $F(r)$ becomes a superposition of the two Bessel functions. The expressions for the electric potential and current density are:

$$\frac{\phi(r, z)}{\phi_0} = \cos(\gamma z) \left[K_0(\gamma r) + \frac{K_1(\gamma r_{\max})}{I_1(\gamma r_{\max})} I_0(\gamma r) \right] \quad (\text{S11})$$

$$\frac{j_r(r, z)}{\phi_0 \gamma \sigma} = \cos(\gamma z) \left[K_1(\gamma r) - \frac{K_1(\gamma r_{\max})}{I_1(\gamma r_{\max})} I_1(\gamma r) \right], \quad (\text{S12})$$

where I_0 and I_1 are the Bessel-I functions of the zero-th and first order. In the limit of $r_{\max} \gg \gamma^{-1}$ the solution coincides with that for an infinite contact pad. The resistance of the contact pad of Fig. 2 is given by:

$$R_c = \frac{1}{\theta \sigma t x_0} \frac{K_0(x_0) I_1(x_{\max}) + I_0(x_0) K_1(x_{\max})}{K_1(x_0) I_1(x_{\max}) - I_1(x_0) K_1(x_{\max})}, \quad (\text{S13})$$

where $x_0 = \gamma r_0$ and $x_{\max} = \gamma r_{\max}$ and θ in the denominator takes into account the angular width of the horn. For $x_0 \ll x_{\max}$, $K_1(x_0) I_1(x_{\max}) \gg I_1(x_0) K_1(x_{\max})$ and the Eq. (S13) simplifies:

$$R_c = \frac{1}{\theta \sigma t x_0} \left[\frac{K_0(x_0)}{K_1(x_0)} + \frac{I_0(x_0) K_1(x_{\max})}{K_1(x_0) I_1(x_{\max})} \right] \quad (\text{S14})$$

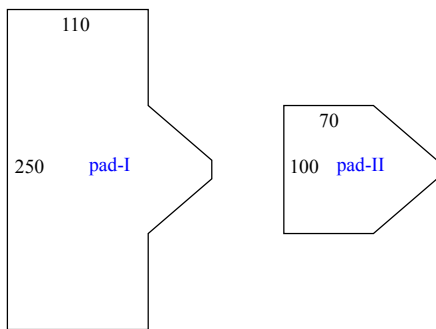
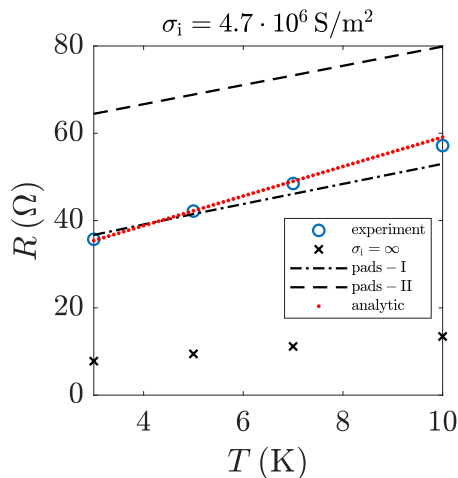
For $x_{\max} \gg 1$ the contact pad size is much larger than γ^{-1} and the second term in the brackets vanishes exponentially. In this case the result for R_c reproduces (S9) with θ instead of π in the denominator, which is a result of reduced angular width. More interesting is the case the pad size smaller than the current transfer length, $x_0 \ll x_{\max} < 1$. Using the asymptotic approximations $I_0(x_0) \approx 1$, $K_0(x_0) \approx \ln(1.12/x_0)$, $K_1(x_0) \approx 1/x_0$, $I_1(x_{\max}) \approx x_{\max}/2$ and $K_1(x_{\max}) \approx 1/x_{\max}$, we find:

$$R_c = \frac{\rho}{\theta t} \ln\left(\frac{1.12}{\gamma r_0}\right) + \frac{1}{A_c \sigma_i}, \quad \text{with } A_c = \theta r_{\max}^2 / 2 \quad (\text{S15})$$

Expression (S15) shows that the resistance of a contact pad with $r_0 \ll r_{\max} < \gamma^{-1}$ has an extra contribution equal to the total interface resistance of the pad with the area of A_c . It is easy to see, that for $\sigma \rightarrow \infty$ ($\rho \rightarrow 0$) one has $\gamma \rightarrow 0$ and (S15) reduces to $R_c = (A_c \sigma_i)^{-1}$, that is the contact resistance between two ideal conductors is controlled solely by the interface resistance.

V. NUMERICAL MODELING

Finite interface resistance could explain substantial deviation in resistivity of two nanowire devices in Ref. [Liyang Chen et al., Science **382**, 907 (2023)]. The resistivity of the 0.66 μm long wire is roughly an order of magnitude higher, as compared to the 28 μm long wire. Based on their response to the temperature and magnetic field similar to those of the parent film it is argued that



Supplemental Material Fig. 3. (upper panel): T -dependence of the resistance in a smaller wire. Circles mark the measured resistance and crosses correspond to $R_0 = \rho L/(wt)$, expected from the resistivity measured in the $28 \mu\text{m}$ long wire under the assumption of ideal interface ($\sigma_i = \infty$). The theoretical fits take into account the contact resistance via $R = R_0 + 2R_c$. Red dotted line is the analytical result (S13) for $r_0 = w/2$, $r_{\text{max}} = 500 \mu\text{m}$ and $\theta = \pi/2$. Black lines are numerical simulations for the contact pads designs pads-I and pads-II. (lower panel): sketches of the designs used in numerics.

this deviation is not a result of the contact resistance. The above calculations indicate that this argument has a caveat.

As follows from (S10), the resistance of an infinite contact pad with a poor interface between the layers has nearly identical to the parent material temperature (T) response, since $R_c \propto \rho$ up to an unimportant log-factor. The same is expected to hold also for the magnetic field

response. For a finite pad a constant resistance offset is present, according to (S15). We have performed numerical calculations of realistic device layouts in order to understand possible effects of the interface conductivity and contact area on the temperature dependence of the resistivity in the smaller nanowire.

Fig. 3 (upper panel) shows the T -dependence of the resistance of the smaller wire with dimensions $L = 0.66 \mu\text{m}$ (length), $w = 0.24 \mu\text{m}$ (width) and $t = 60 \text{ nm}$ (film thickness). Circles mark the measured resistance and crosses correspond to $R_0 = \rho L/(wt)$, expected from the resistivity measured in the $28 \mu\text{m}$ long wire under the assumption of ideal interface ($\sigma_i = \infty$). This data is obtained by digitizing the published data. In order to capture the experimental behavior of the smaller wire we performed numerical simulations for two sizes of the contact pads, shaped as close as possible to the original design. The designs of a bigger (pads-I) and smaller (pads-II) contact pads are shown in the lower panel of Fig. 3. Numerical results are shown in Fig. 3 by dashed-dotted and dashed black lines, respectively, both obtained assuming the interface conductance of $\sigma_i = 4.7 \cdot 10^6 \text{ S/m}$. The values of σ_i, ρ and t correspond to the current transfer length of $\gamma^{-1} \approx 280 \mu\text{m}$, which is comparable to the size of pads-I and considerably larger than the size of pads-II. The total device resistance $R = R_0 + 2R_c$ is much larger than R_0 (crosses) and exhibits sizable T -dependence, comparable to the experiment (circles). The resistance is larger for pads-II, as expected for their smaller area according to (S15). Moreover, the experiment is consistent with the prediction of (S13) for $r_0 = w/2$, $r_{\text{max}} = 500 \mu\text{m}$ and $\theta = \pi/2$, see the red dotted line. Altogether, we find that poor interface quality can well be responsible for the unexpectedly high resistance of the smaller device.

VI. SUMMARY

We observed that in the two-dimensional case the resistance of a contact pad caused by poor interface quality scales nearly proportional to the resistivity of a parent film. This could explain deviations in resistivity values between the larger and smaller devices in the experiments of Ref. [Liyang Chen et al., Science **382**, 907 (2023)]. The observation has important consequence for the interpretation of shot noise data in a smaller wire, since the effective length of the device may exceed the electron-phonon relaxation length. In this situation the observed reduction of the shot noise may not be surprising.